Extracellular matrix and spores impart structural hierarchy and compositional heterogeneity in Bacillus subtilis biofilms.

David N. Azulay[1,7#], Oliver Spaeker[2#], Mnar Ghrayeb[1,7], Michaela Wilsch-Bräuninger[3], Ernesto Scoppola[2], Manfred Burghammer[4], Ivo Zizak[5], Luca Bertinetti[6], Yael Politi[6]* and Liraz Chai[1,7]*

[1] Institute of Chemistry, The Hebrew University of Jerusalem, Edmond J. Safra Campus, Jerusalem 91904, Israel
[2] Department of Biomaterials, Max Planck Institute of Colloids and Interfaces, 14476 Potsdam, Germany
[3] Max Planck Institute of Molecular Cell Biology and Genetics, 1307 Dresden, Germany
[4] European Synchrotron Radiation Facility (ESRF)71, avenue des Martyrs, CS 40220, Grenoble Cedex 9 38043, France
[5] Helmholtz-Zentrum Berlin, Department Structure and Dynamics of Energy Materials, Berlin, Germany
[6] B CUBE - Center for Molecular Bioengineering, Technische Universität Dresden, Dresden, Germany
[7] The Center for Nanoscience and Nanotechnology, The Hebrew University of Jerusalem, Edmond J. Safra Campus, Jerusalem 91904, Israel

# equal contribution

* *To whom correspondence should be addressed: Dr. Liraz Chai, Institute of Chemistry, The Hebrew University of Jerusalem, Edmond J. Safra Campus, Jerusalem 91904, Israel. Telephone: +972-2-6585303, Fax. +972-2-5660425. Email. Liraz.chai@mail.huji.ac.il; Dr. Yael Politi, B CUBE - Center for Molecular Bioengineering, Technische Universität Dresden, 01307 Dresden, Germany. Email. yael.politi@tu-dresden.de*

Abstract

Biofilms are surface-associated soft microbial communities that may be beneficial or detrimental to their hosting environment. During biofilm development, cells protect themselves with polymeric matrix, termed the extra-cellular matrix (ECM), and organize in space into functionally distinct subgroups, in a process resembling differentiation in higher organisms. An interesting question arising is whether this division of labor in biofilms is also reflected in the molecular-level order across whole biofilms. Using combined X-ray diffraction/fluorescence, we studied the molecular order in intact biofilms. We discovered that biofilms display a distinct spatio-temporal XRD signature that depends on highly ordered structures in spores and on cross-β sheet structures in matrix components. Furthermore, signals of spores, water molecules and metal-ions are especially enhanced along macroscopic wrinkles, known to act as water channels. Demonstrating *in situ* the link between molecular structures, distribution of metal-ions, and division of labor across whole biofilms in time and space, this study provides novel insight that is crucial for better understanding of biofilm development and physiology.

Introduction

Biofilms are soft microbial communities that form on surfaces and at interfaces [1,2]. Bacterial biofilms are composed of vegetative cells that are embedded in a network of secreted polysaccharides, proteins and nucleic acids, termed the extracellular matrix (ECM)[3]. The ECM network provides biofilms with diverse essential properties [4], endowing mechanical stability [5,6], regulating spreading [7] and osmotic pressure [8], water and mineral uptake [9], providing a hydrophobic shield [10,11], affecting the precipitation of minerals such as calcium carbonate [12,13] and increasing the resistance of the biofilm cells to antibiotic activity [4,14]. Under physiological stress conditions, cells in biofilms from the *Firmicute* phylum, such as *Bacilli* and *Clostridia*, form dormant spores, where the genome is stored in a partially dehydrated core, surrounded by a protective coat made of organized proteins and glycoproteins [15-18]. Biofilm spores often reside in aerial structures, projecting from the biofilm's surface, which facilitates their dispersal [19,20].

Biofilm research has been stimulated by the realization that nomadic bacterial cells often adopt a communal form of life [21,22]. Molecular genetics approaches to biofilm research yielded genetic pathways that are involved in biofilm formation [23], studies of quorum sensing within biofilms provided insights into the molecules used by cells for communication [24-27], and biochemical studies generated compositional and structural knowledge of ECM isolated components [10,11,28-32].

An emerging perspective of biofilm development considers them as multicellular organisms because of their ability to differentiate into subgroups of cells expressing specific set of genes. In particular, differentiation in *B. subtilis* biofilms has been shown to give rise to distinct, function-related subpopulations, among which are motility, matrix production, sporulation [20,33] and cannibalism [34,35]. Heterogeneous matrix gene expression has also been linked to heterogeneity in the mechanical robustness of subpopulations [36,37]. Current views of differentiation of biofilms into subgroups therefore link genetic division of labor and phenotypic heterogeneity at the single cell as well as the

subpopulation level, however, they neglect a molecular view of structural and compositional heterogeneity across entire biofilms.

We hypothesized that the division of labor across biofilms may lead to molecular ordering within specific domains in the biofilm. To test this hypothesis, we studied the local molecular structure and elemental composition across biofilms in a spatially resolved manner. We used micro-focus X-ray diffraction (XRD) and X-ray fluorescence (XRF) to scan along intact biofilm samples of different ages, using *B. subtilis* as a model organism for biofilm formation. XRD revealed that the internal spatio-temporal division of labor in *B. subtilis* biofilms is manifested by structural profiles that depend mainly on the presence of spores, ECM components and the presence of free and bound water molecules. Spores displayed a highly ordered structure, while ECM conveyed minimal cross-β sheet structure, that only partially depended on the presence of the major proteinaceous ECM component, TasA. XRF measurements exposed variable preference of biofilms, ECM components and spores to metal ions, mainly calcium, magnesium, manganese, iron and zinc. Our study provides a comprehensive multiscale molecular view of multicellularity in biofilms, demonstrating a link between biofilm morphology, molecular structure and metal ions preference that mirrors the division of labor of subgroups across whole biofilms *in situ*.

Results

Spore-component XRD contribution dominates the diffraction pattern of mature *Bacillus subtilis* biofilms.

Scanning XRD/XRF with a microfocused X-ray beam is a powerful tool allowing to probe the local molecular structure of a heterogeneous sample with high spatial resolution. We scanned a (2.6 x 6) mm^2 area of an intact sealed and hydrated biofilm using a micro-focused X-ray beam while simultaneously acquiring XRD and XRF, as described in the schematic presented in Fig. 1. We chose a mature WT biofilm sample (10 days old) where mm-scale, dominant morphological wrinkles were

preserved during sample preparation (Fig. 1). For each pixel along the scanned region (X-ray beam cross-section = (50x50) μm^2, step size = 200 μm, 300 μm on X, Y axes, respectively), we simultaneously obtained a two-dimensional (2D) diffraction pattern collected on an area detector and an XRF spectrum. The 2D patterns were mostly completely isotropic (see for example the 2D diffraction pattern in Fig. 2A), indicating that within the biofilm plane there was no preferred alignment of structural components. We therefore azimuthally integrated the 2D patterns (in the full range 0-360°) to obtain a one-dimensional (1D) profile of the intensity (*I*) versus scattering vector (*q*). Peaks on the 1D profile correspond to reflections from ordered structures in the biofilm, with characteristic *d*-spacings (units of length) in real space inversely related to *q* ($d = 2\pi/q$).

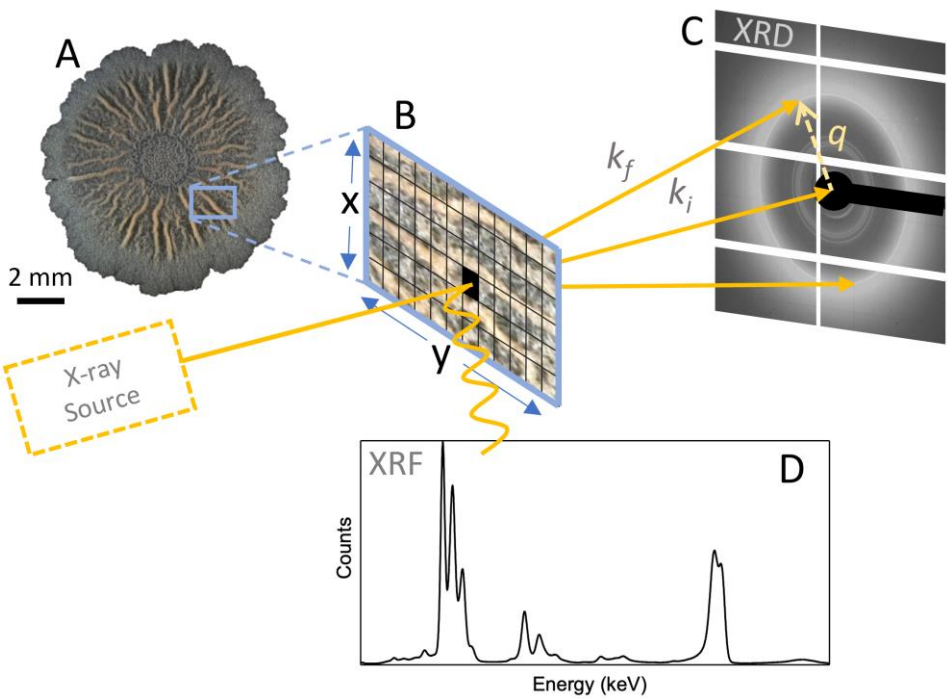

Fig. 1: Schematic representation of the experimental set-up. A slice (B) from an intact biofilm sample (A) is placed between an X-ray source and a two-dimensional area detector (C) in transmission geometry. XRD signal is collected simultaneously with X-ray fluorescence (XRF) using a fluorescence detector (D) located almost perpendicular to the incoming beam. The X-ray beam scans the sample in pre-set step sizes along the x and y directions, defining pixels of x*y areas (see for example the black colored pixel in (B)). Scanning over large area provides structural and compositional information with spatial resolution that is determined by the size of the beam cross section and the scanning step size. k_i and k_f are the direct beam and scattering vectors, respectively. *q* is the defined as the difference between k_f and k_i. The image is not drawn to scale and the pictures used are for illustration purposes only. Random areas in the biofilm are mapped in each biofilm during an experiment.

The diffraction patterns of the intact, hydrated, 10 days old wild-type (WT) biofilm sample showed scattering signals in both low (q = 5 nm^{-1} to 8 nm^{-1}) and high (q = 10 nm^{-1} to 29 nm^{-1}) q-ranges (Figs. 2A-C). In the low q range (marked with a blue arrowhead in Figs. 2A, 2B and a rectangle in Fig. 2C), WT biofilms exhibited several reflections, residing around ~ 6 nm^{-1}, corresponding to structural order with d-spacing in the order of 10 Å in real-space, which typically contained a sharp doublet superimposed on a broader hump (Fig. 2D, Tables S1, S2).

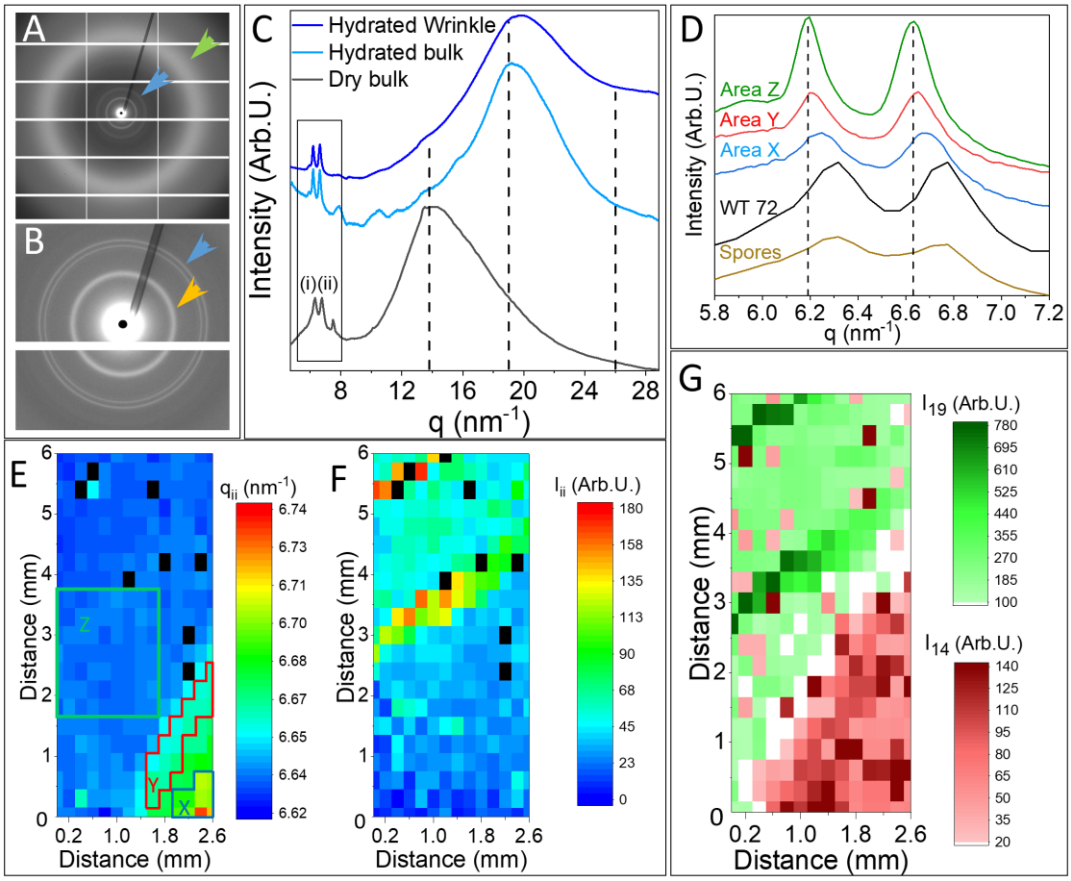

Fig. 2: **XRD of an intact hydrated and fixed-dry WT biofilm.** (A) Full detector image showing a characteristic 2D pattern obtained from a natively hydrated biofilm, green arrowhead shows the water scattering signal, (B) Zoom-in into the low q range, showing the dominant doublet (marked with a blue arrowhead in A and B); Orange arrowhead marks the sample carrier (polyimide film) signal. White grid lines are gaps between detector units. (C) Representative azimuthally integrated 1D diffraction profiles of a native hydrated (dark and light blue curves taken from a wrinkle and bulk region, respectively) and fixed-dry (black curve) biofilms. The profiles show a

doublet peak in the low *q* range (marked with rectangle and corresponding to the blue arrow in (A, B)) and broad signals in the high *q* range (marked with green arrowhead in (A)). Dashed lines point at peak positions q = 13.8 nm^{-1}, attributed to biofilm biopolymers, and q = 19 nm^{-1}, 26 nm^{-1}, attributed to water scattering signal. (D) Zoom into the low *q* range (marked with a rectangle in (C)), showing the average profiles in different areas in the biofilm sample (X, Y, Z, in (E) corresponding to the blue, red, green curves, respectively), the average profiles in a fixed and dry biofilm (black curve) and in a spore (dry) sample (olive green curve). (E) Mapping of the *q* position of the low *q* peak at ~ 6.7 nm^{-1} (peak (ii), marked in (C)), corresponding to ~ 9.4 Å d spacing, across a WT biofilm slice of (2.6 x 6) mm^2 area. (F) Intensity maps of peak (ii) showing higher intensity along biofilm's wrinkles. (G) Mapping the intensity of the dominant peaks in the high *q* range, q = 14 nm^{-1} and q = 19 nm^{-1} highlight the drying versus hydrated areas, respectively; Water scattering signal at 19 nm^{-1} is highest along the biofilm wrinkles, which serve as water channels [38].

The XRD pattern of dry WT biofilms largely corresponded to the XRD profile reported before for isolated spore samples [39], and confirmed by us (Figs. 2D and S1). The relative intensities of the two peaks comprising the doublet were similar across the biofilm sample (Fig. S2C), implying that they originate from a single spore-component or from components with similar relative abundance.

We used peak-fitting to evaluate the variation in specific reflections across the sample, yielding peak position, width and amplitude for the dominant scattering signals for each of the measured pixels (position in the biofilm) (Fig. S3, Tables S1, S2). Mapping the spatial variation of the dominant doublet reflections in the biofilm showed that the doublet appeared across the whole biofilm sample, with the *q* values ranging between 6.19 to 6.24 nm^{-1} (peak (i), Fig. S2A) and 6.70-6.63 nm^{-1} (peak (ii), Fig. 2E). The doublet peak positions were rather uniform across the measured area, yet they exhibited a small gradient, shifting to higher *q* values along the direction going from the top left corner of the biofilm sampling area to the bottom right (Fig. 2E). The intensity of the doublet showed an increase along large wrinkles in the biofilms relative to areas away from or between the wrinkles (Fig. 2F).

Biofilm hydration state reflects biofilm morphology

In the high *q* range, the diffraction profiles of the hydrated sample showed typically broad peaks that we deconvoluted using peak-fitting (Fig. S4). In all the biofilms we tested, namely, fixed and dry (curve 'dry bulk' in Fig. 2C), as well as natively hydrated biofilms ('hydrated bulk' and 'hydrated wrinkle' in Fig. 2C), the broad peak included contributions around 14 nm^{-1}, corresponding to reflections from biopolymers present in the ECM and to ordered structures inside the cells. The sugar-phosphate backbone in DNA, for example, which is present both inside and outside the cells in the biofilm [40], gives rise to a characteristic reflection at 15 nm^{-1} [41] and polysaccharides purified from biofilms showed typical scattering at q ~ 13 nm^{-1} (Fig. S5). In addition to the contribution at q ~ 14 nm^{-1}, native hydrated biofilms had contributions around q = 19 nm^{-1} and q = 26 nm^{-1}, corresponding to scattering from water [42,43]. Previous reports have shown that hydration layers in proteins give rise to scattering signal around q = 19 nm^{-1} [42], while free, liquid water give rise to reflections at q = 19 nm^{-1} as well as q = 26 nm^{-1}, originating from the hydrogen bonding of water with typical distance of between oxygen atoms around 2.8 Å [43]. Strikingly, the relative contribution of these reflections depended on the position in the biofilm. In pixels located directly at wrinkles (curve ' hydrated wrinkle' Fig. 2C), free water (q = 19 nm^{-1} and 26 nm^{-1}) contributed the most to the high q range. In fact, fitting results show that the relative amplitude of these two peaks is comparable to that of pure liquid water (Table S1, Fig. S4). In bulk areas away from the wrinkles (curve 'hydrated bulk'), the free water signal at 26 nm^{-1} was diminished (Figs. 2C and S4), leading us to conclude that the contribution at q ~ 19 nm^{-1} results from water bound to ECM biopolymers. This finding stands in agreement with a previous study, that showed that biofilm wrinkles serve as channels filled with water and essentially function to transfer nutrients across biofilms [38]. In biofilms aged older than 6 days, these channels become closed tubes [38], which can explain the entrapment of free water that we observe with XRD in the 10 day old biofilm section that was removed from its original substrate.

Interestingly, the large spatial variation in the intensity of the water signal (Fig. 2G) reflects dehydration during the measurement period. This dehydration provided an interesting insight into hydration/dehydration processes in biofilms. Mapping the intensity of the peak contributions in the high *q* range across the sample (Fig. 2G) revealed that the 14 nm^{-1} reflection was dominant in the top left part of the sample and that of the 19 nm^{-1} at the bottom right part of the sample. In the hydrated regions (with high water scattering signal), the 14 nm^{-1} peak was still visible but partially obscured by the presence of the broad intense 19 nm^{-1} peak (water signal). The dehydration gradient spanning along the diagonal of the biofilm sample coincides with shifting of the spore-related doublet peak position to larger *q* values (i.e., smaller atomic separations), as shown in Fig. 2D, 2E. In fixed dry samples of 72h WT biofilms and in isolated spore samples (Fig. 2C), these peaks show up at their largest *q* positions (6.3 nm^{-1} and 6.8 nm^{-1}), corresponding to smallest molecular separations (d spacings). This observation is in agreement with a suggestion that the doublet signal is attributed to highly organized spore coat proteins [16,39,44,45] and therefore sensitive to biofilm hydration. An intriguing hypothesis then arises that spore coat protein swelling may serve as humidity sensors for spore germination.

Metal ions preferentially accumulate along biofilm wrinkles

We measured the XRF signal from biofilms concurrently with XRD in order to probe the distribution of accumulated metal ions across biofilms (Fig. 3). The fluorescence photon counts were then converted to relative atomic density taking into account the energy dependent absorption cross-section for each element [46-49]. While Ca was by far the most abundant metal ion in all samples, we found an interesting spatial distribution for Zn, Fe and Mn with increased signals along the biofilm wrinkles. A similar trend was observed for Mg (Fig. S2D), however the signal to noise in this measurement was relatively low due to the low fluorescence emission energy of Mg leading to significant absorption in air. For comparison, the distributions of Ca and K (Fig. 3, Fig. S2E, respectively) did not correlate with the wrinkle morphology.

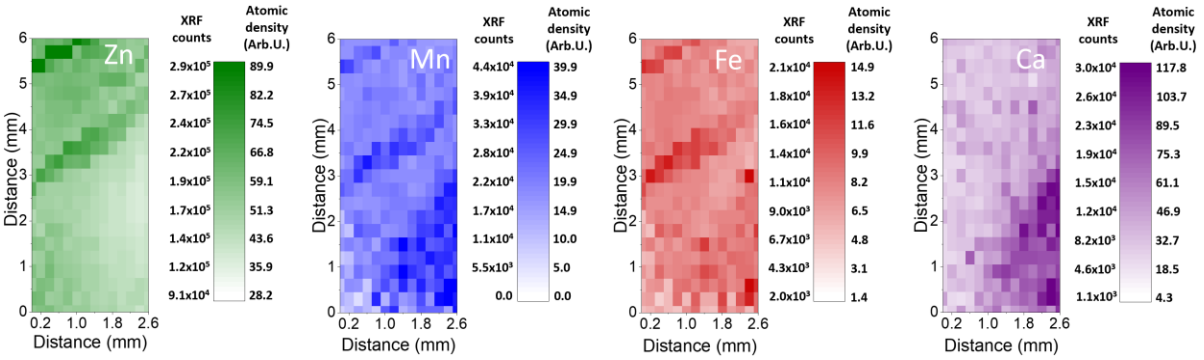

Fig. 3: **Atomic density measured by XRF of intact hydrated WT biofilm slice**. XRF/Elemental distribution maps are plotted for each metal ion. The LUT describes the XRF counts (values to the left of the scale) and the corrected fluorescence signals (values to the right of the scale) of Zn (green), Mn (blue), Fe (red), Ca (magenta) of WT biofilms. The signal of Zn, Mn, and Fe, but not Ca, is stronger in the biofilm wrinkles, coinciding with water and spore accumulation along biofilm wrinkles.

The elevated signal of Zn, Mn, and Fe coincided with increased intensity of the spore-related doublet XRD signature and water scattering acquired simultaneously. One possible explanation to the increased XRD signal along the wrinkles could be that the biofilm is thicker along wrinkles, however, this effect alone would lead to an increase of the XRF signal of all the metal ions. The uniform Ca and K signals across the biofilms, makes this possibility less probable.

While the XRF signal cannot be quantified into absolute values, after corrections for the absorption cross-section, the relative abundance of metal ions can be compared to obtain the general trend of ion abundance. We therefore evaluated the atomic abundance of Zn, Mn, and Fe relative to the most abundant Ca in areas positioned at the biofilm bulk (away from the wrinkles) and compared them to the relative concentrations of these metal ions in the medium (Table S3).

Ca accumulation is enhanced relative to the other metals ions, even after considering its higher abundance in the medium (Table S3). This suggests that calcium is preferentially bound in the biofilm thus maintaining a high concentration gradient relative to the medium. Ca binding by the ECM was already shown before, and suggested to stabilize the biofilm and inhibit biofilm dispersal [50]. In

contrast, Zn, Mn, and Fe are more free to diffuse and flow as solutes in water channels. We hypothesize that these metal ions accumulation along wrinkles where evaporation in enhanced [38]. Strikingly, the relative abundance of Zn, Mn, and Fe with respect to Ca, is similar in ECM mutant biofilms and in the bulk of WT biofilms. ECM mutants don't have wrinkles [3], which may be explain the lack of localized metal ion accumulation in these biofilms.

The co-occurrence of metal ions, water channels and spore accumulation raise an interesting question, whether the enhanced evaporation of water along the wrinkles lead to salt accumulation that in turn triggers sporulation in these positions. At the same time, spores may serve as metal ions reservoir, thereby regulating salt concentrations that may otherwise become toxic. Indeed, isolated spore samples (Fig. S6), showed accumulation of the same metal ions (Ca, Zn, Mn, and Fe), which have been described to play a role in sporulation [50-52].

Loss of spore-associated reflections exposes weak cross β sheet structure in matrix mutants and in young biofilms

Assigning the XRD doublet to spores, we studied matrix mutant biofilms, Δ*tasA* and Δ*eps*, reported to negligibly express sporulation genes [20]. Transmission electron microscopy (TEM) imaging of WT biofilms (Figs. $4A_{ii} - 4A_{iv}$) and mutant biofilm samples (Figs. $4B_{ii}$-$4B_{iv}$, $4C_{ii}$-$4C_{iv}$), reveal several cell types, in particular, normal cells (examples marked with orange arrows), lysed cells (examples marked with blue arrows), deformed cells (examples marked with yellow arrows), sporulating cells (examples marked with green arrows) and spores (examples marked with purple arrows). The TEM images in Fig. 4, as well as a quantitative analysis of the cell types in different TEM images (total number of cells was 4715 in a total of 189 images) (Fig. 4D) show clearly that the abundance of sporulating cells and spores in biofilms made by the ECM mutants, Δ*eps* and Δ*tasA*, is negligible relative to their abundance in WT biofilms.

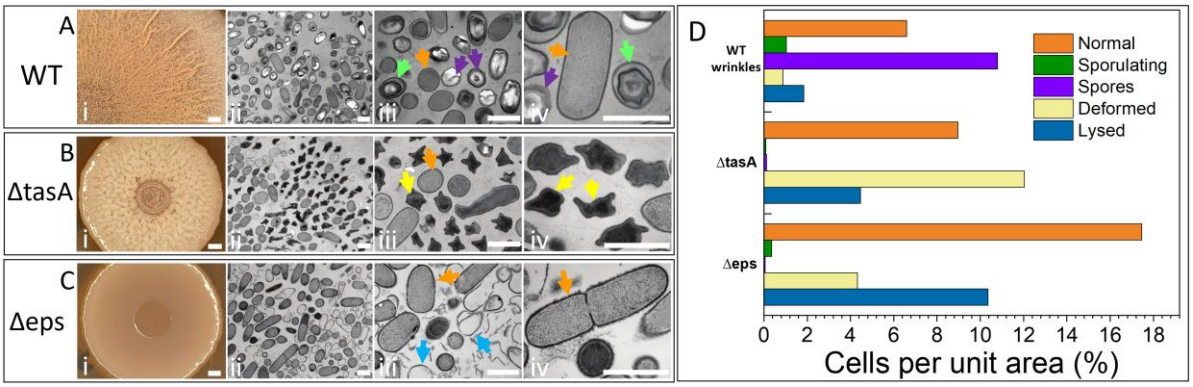

Fig. 4: **Cell type abundance in WT and matrix mutant biofilms**. (A_i, B_i, C_i) Light microscopy of biofilm samples and TEM imaging of fixed and stained thin sectioned WT (A_{ii} - A_{iv}), Δ*tasA* (B_{ii}-B_{iv}) and Δ*eps* (C_{ii}-C_{iv}) mutant biofilms. We identified several cell types in the TEM images: normal cells (marked orange), lysed cells (marked blue), deformed cells (marked yellow), sporulating cells (marked green) and spores (marked purple). Scale bar in all panels is 1 µm. (D) Quantitative analysis of the cell types observed in TEM images, as shown in Figs. $4A_{ii}$-$4A_{iv}$, $4B_{ii}$-$4B_{iv}$, $4C_{ii}$-$4C_{iv}$. Number of cells, normalized by unit area (unit area = 28.14 mm^2 is the area of a single image). Cell types were identified and numbered as explained in the text and in the Experimental section.

The stark reduction in spore and the increased numbers of lysed cells in ECM mutant biofilms (Fig. 4), suggest increased cannibalism in matrix mutant biofilms, as previously proposed [35]. Furthermore, if spores indeed accumulate metal ions, their absence may lead to toxic accumulation which in turn increases cell death.

The 1D XRD profiles (Fig. 5) showed loss of the spore-associated doublet in Δ*tasA* mutant biofilms (burgundy curve in Fig. 5). We observed two typical profile types for the Δ*eps* mutant biofilms. In one profile type, the double peak disappeared altogether (orange curve in Fig. 5) while in the second type, it was apparent as low intensity peaks superimposed on top of a broad hump (brown curve in Fig. 5). Combined with the TEM images presented in Fig. 4, the loss of the spore-associated doublet XRD peak is therefore related with the loss of spores in biofilms of the matrix mutants. Profiles lacking the dominant spore-associated reflections exposed XRD patterns that originated from other components in the biofilm, namely cells and matrix components. Interestingly, we identified in these profiles the two broad reflections appearing at q ~ 6 nm^{-1} and ~ 14 nm^{-1}, that typically correspond to the canonic cross β structure attributed to a 10 Å (intrasheet) and 4.7 Å (interstrand) spacings, respectively [53].

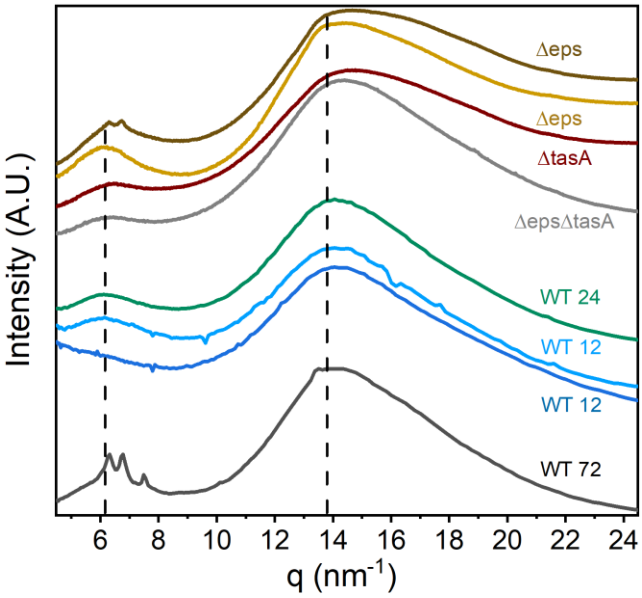

Fig. 5: **Comparison of the XRD of mature WT biofilms, young biofilms and ECM mutant biofilms**. XRD of fixed mature (72 h old) WT biofilms, fixed mature biofilms made by matrix mutant cells Δ*eps* and Δ*tasA*, double mutant Δ*eps*Δ*tasA*, as well as by fixed young biofilms (aged 12 h and 24 h), where spores have not yet developed. Dashed line marks the position of the inter-sheet and intra strand peaks in cross β sheet structures (q ~ 6 nm^{-1} and 14 nm^{-1}).

We hypothesized that TasA, the most abundant structural protein in *B. subtilis* matrix [28], is the major contributor to the cross-β sheet signal in the biofilm, because its crystal structure contains a cross- β sheet core[54], and it is suggested to form amyloid fibers *in vitro* [28,30,54]. Indeed, while all the mutant biofilms measured contained the low and high peak contributions, the relative intensity of the low peak contribution (namely around 6 nm^{-1}), was lower in mutants that lacked TasA (burgundy curve, Fig. 5).

The mutant biofilms described above were poor in spores, but they additionally lacked either the protein matrix component, TasA, the polysaccharide matrix component, EPS, or both. In order to test this hypothesis, we performed a temporal analysis of the biofilm XRD at early time points, namely at 12 h and 24 h, where according to Vlamakis et al., WT biofilms express TasA to a variable degree, but they do not yet produce spores [20]. XRD profiles indeed showed that the spore-associated doublet, was not yet present in young biofilms. At 24 h, broad peaks appeared (green curve, Fig. 5), attesting the

contribution of matrix and cells to the XRD signal. At 12 h, the broad hump around 6 nm^{-1} was occasionally present, but in other regions the low q range did not contain any signal. Indeed, at 12 h *tasA* expression is initiated but the matrix is not yet uniform across the whole biofilm area (cyan and blue curves, Fig. 5) [20]. Probing the samples at this time point allowed to isolate the XRD signature of cells with little contribution of the matrix. The loss of the low *q* hump in these biofilms indicated that higher order intramolecular structures, associated with inter-sheet signature in weak cross β structure, are dependent on the presence of matrix components and that the cells themselves do not contribute to the signal at low *q*.

XRD data of WT biofilms of different age and matrix mutant biofilms were fitted with five peak positions covering the low and high *q* ranges (see Tables S1, S2, and Fig. S3) in order to compare the dominant peak positions. For simplicity, we only specify here the low *q* peak position without the doublet, and two peak positions in the high *q* range (this is a broad hump and a shoulder and therefore two positions were necessary to represent it). Both the low and high *q* peak positions, attributed to cross β structures, were similar in fixed mature WT, matrix mutants (Δ*eps*, Δ*tasA* and Δ*eps*Δ*tasA*) and, when present, in young biofilms (see dashed lines in Fig. 5 located in the peak positions of the inter-sheet and intra strand peaks in cross β sheet structures (q ~ 6 nm-1 and 14 nm-1)). While the cross β signature was more dominant in biofilms containing TasA, similar cross β sheet signature was found also in biofilms made by *tasA* mutants (grey and burgundy curves in Fig. 5). We thus conclude that intact biofilms harbor a cross β sheet structure resulting from matrix components not limited to TasA.

TasA harbors a minimal cross-β domain and binds metal ions

Facing the presence of cross β sheet fingerprint in intact biofilms, its increase in the presence of TasA (in 24 h and 72 h WT samples) and in light of the literature debate on the amyloid nature of TasA [28,31,54,55], we were intrigued to learn more about the structure and composition of fibers formed *in vitro* from isolated TasA preparations. Recently, we have shown that TasA is polymorphic, as it forms fibers with different morphologies: aggregates in acidic solutions (termed 'aggregates' henceforth),

fiber bundles at high protein and salt concentration (termed 'bundles' henceforth) and thin and long fibers at high salt concentrations (termed 'fibrils' henceforth). [30,56,57].

To examine a possible relation between binding of metal ions by TasA and by biofilms, we examined protein fibers preparations with XRF. XRF maps of the dominant metal ions, Ca, Zn, Fe, and Mn (Figs. 6A-6F, Figs. S7, S8) revealed that TasA fibers contained mostly Ca (Figs. 6A,6C and 6E), but also the metal ions Zn, Fe and in some cases Mn, that were also probed in WT and mutant biofilms (as shown in this and in other studies [9]) (Figs. 6B, 6D, 6F). However, different TasA polymorphs showed different preference to these metal ions as shown in an overlay of the XRF maps of these metal ions (Figs. 6B,6D,6F and Fig. S7). In particular, in aggregates that formed in an acidic environment, iron binding dominated over Mn and Zn (Fig. 6B), whereas bundles that formed in high salt (NaCl) and protein concentrations accumulated more Zn relative to Mn and Fe (Fig. 6D, S7). The fibrils that formed at high salt concentration were especially heterogeneous, as was reflected both in different morphologies and in metal ion binding preferences residing in the same sample (Fig. 6F).

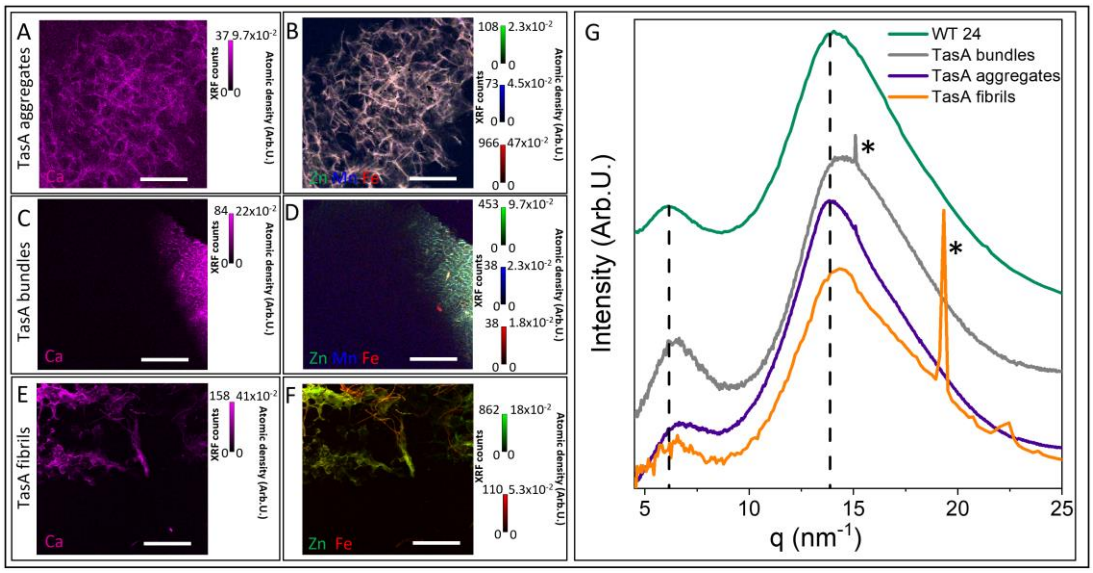

Fig. 6: Morphology, metal ion binding and XRD profiles of TasA fibers formed in different environments. (A-F) XRF of TasA fibers, formed in acidic conditions ('TasA aggregates), high protein and salt concentration ('TasA bundles') and high salt concentration ('TasA fibrils'). XRF maps of Ca (A, C, E) are presented separately from the overlay of the XRF maps of Zn, Fe, and Mn (B, D, F) due to its higher abundance (atomic density) in all the samples. Color code: Ca (magenta), Zn (green), Mn (blue) and Fe (red); red and green = yellow. (G) XRD profiles of TasA aggregates (purple curve), fibrils (orange curve), and bundles (grey curve) along with the XRD profile of 24 h old WT biofilms (green curve). The sharp peaks in the fibrils' profile, marked with * formed at high NaCl concentration are attributed to salt crystal impurities. Scale bar represents 300 µm.

In these fibers, Fe (red) binding was observed within long fibers with high persistence length, while Fe, Zn and Ca appeared to be distributed inhomogeneously in larger areas where the fibers assembled into a mesh (red and green appear as yellow). These results suggest that at least part of the metal ions in biofilms, especially Ca, are bound by TasA within the matrix. The variations in the XRF signal of TasA fibers, prepared under three different environmental conditions, is a further testimony of the protein's polymorphism.

Fig. 6G shows the averaged 1D azimuthally integrated XRD signatures of isolated TasA that formed fibers *in vitro* under these three conditions. The XRD profiles of the three preparations of TasA fibers exhibited two broad reflections close to q ~ 6 nm^{-1} and ~ 14 nm^{-1}, corresponding to the canonic cross β sheet structure. Peak-fitting shows that these peaks were slightly shifted to higher q, relative to those of 24 h old WT biofilms (marked by vertical dashed lines, see also Table S1), indicating a more compact packing of TasA fibers formed *in vitro* relative to biopolymers within the biofilm.

Diehl and co-workers reported XRD patterns of TasA fibers formed from recombinant protein in acidic conditions displaying narrow intra-sheet and inter-strand reflections of a cross β sheet configuration [54], which, in our case, are very broad. While the combination of these two reflections is indicative of cross β sheet features, it is unlikely that they organize into long range ordered amyloid structure in our case. This is consistent with our previous suggestions that TasA fibers form in a oligomer-to-oligomer addition [57], but our data is insufficient to suggest a model for the interactions between monomers and/or oligomers. We attribute the disparity in the molecular organization of TasA fibers between that reported here and that demonstrated for amyloid fibers to the fact that our fibrils are composed of full length proteins, rather than short peptides [53,58-60] or truncated (recombinant) sequences [54]. Considering the NMR studies and crystal structure of TasA as being composed of β strands arranged in a jelly roll core, as well as alpha helices and loops [54], the cross- β structure may arise from the internal core or from packing of intermolecular β strands or sheets. Importantly, the similarity between the XRD patterns of TasA fibers formed *in vitro* and the matrix XRD signal obtained

in situ suggests that in intact biofilms, TasA and other ECM components form ordered fibers that are nevertheless not amyloidogenic.

Discussion

We have performed a comprehensive spatio-temporal analysis of molecular structures within *B. subtilis* biofilms and revealed that spatial differentiation by function also translates into structural and elemental heterogeneity in intact biofilms at the molecular level. Probing intact biofilms with XRD, we have found that *B. subtilis* biofilms convey a structural hierarchy of three characteristic structural signatures (illustrated in the schematic cartoon in Fig. 7).

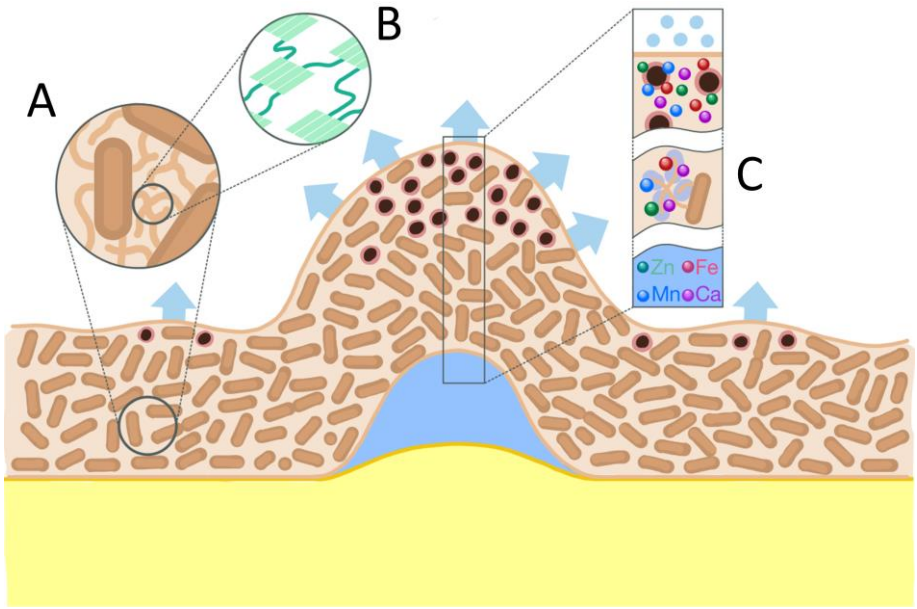

Fig. 7: **Schematic representation of the relationships between biofilm structures and metal ion distribution and their implications on biofilm physiology**. The cartoon shows a side view of a WT *B. subtilis* biofilm, drawn around a wrinkle, and it captures the major findings of this study. We identified three dominant structure-based subgroups in biofilms, vegetative bacterial cells (represented by brown ovals surrounded by an orange coat), spores (represented by dark circles surrounded by a pink coat) extracellular matrix components (represented by a brown mesh surrounding the cells), and a water channel (shown in light blue) residing beneath a biofilm wrinkle. The light blue arrows represent water evaporation. A zoom into the ECM mesh shows ECM fibrillar components (A), and a further zoom in highlights their structure, short cross β sheet domains that are connected with non-cross β sheet regions (B). A column across the biofilm wrinkle (black rectangle) marks the three areas along the biofilm where metal ions reside (we only refer to the metal ions that were observed in this study). Water molecules and metal ions are free inside water channels. They are then adsorbed by the ECM, with Ca being more abundant than Zn, Mn, and Fe. Ca remains mostly bound to the ECM, but Zn, Mn, and Fe are free to diffuse and concentrated in biofilm wrinkles, where water evaporation is the largest, possibly leading to sporulation.

The most conspicuous signature originates from ordered structures within the coat of spores, that are sensitive to the hydration level of the film. The spores are present throughout the biofilm but concentrate along large wrinkles that serve as water channels. The spores' signal is lost in biofilms lacking the matrix components as in Δ*tasA* and Δ*eps*, as well as in young biofilms, where sporulation has not yet been initiated (as also shown by TEM). In the absence of the spore contribution to the XRD signal, the XRD profile of bacterial cells and biofilm extracellular matrix could be revealed. In contrast to the sharp, crystalline-like structured related with the spore-coat, the ECM exhibits a cross β sheet structure that is only partially related with the presence of the protein, TasA. Furthermore, our results show that it is unlikely that full-length TasA fibers possess long range amyloidogenic order either *in vitro* or *in situ*. The third dominant signature in WT biofilms is that of water. Specifically, we observed scattering of water in two states, free water associated with biofilms wrinkles, in agreement with their role as water channels, and bound water in the biofilm bulk. In parallel to the structural information provided by the XRD, we performed concomitant spatial elemental analysis by XRF. We have found that biofilms accumulate mostly Ca, but also Zn, Mn, and Fe, that colocalize with water channels. Metal ions are crucial for bacterial metabolism [61], and they have indeed been associated with bacterial biofilms [62]. Here we tracked their spatio-temporal location in intact and natively hydrated biofilms.

Mapping the XRD and XRF signatures of intact biofilms in space and time allowed us to suggest an inclusive view of biofilm development, linking the ECM and the spores via the transport of metal ions, as illustrated schematically in Fig. 7. We suggest that metal ions initially reside in the medium accumulate in the ECM biopolymers that serve as a selective filter to specific metal ions, especially Ca. This process is driven by water evaporation which occurs throughout the film, but enhanced along wrinkles[38]. Ca is selectively bound by the matrix and is therefore filtered out from the fluid in the water channels. Zn, Mn and Fe, which are only weakly bound by the matrix or taken up by cells, are carried by the water flux in the channels (wrinkles), where they eventually accumulate. The co-occurrence of these metal ions and spores along wrinkles is consistent with their essential role in sporulation [51,63,64]. The relative metal ions abundance in ECM mutant biofilms is similar to that in 72 h WT biofilm bulk, and yet sporulation is detained. This suggests that even though the metal ions are accumulated across the film, the lack of wrinkles and lateral water flow prevents localized accumulation of some metal ions with respect to Ca, and that these altered Ca/metal ion ratios are crucial for sporulation. The ECM in biofilms therefore plays a dual role in biofilm; it provides structural support but also a selective filter for metal ions essential for biofilm development. This hypothesis therefore suggests a functional link between macroscopic features in biofilms to ECM molecular order and cellular differentiation. Multiscale approaches to biofilm internal structures and metal ion relationships may hold a key to the understanding biofilm physiology and multicellularity.

Materials and methods

Bacterial *Bacillus subtilis* strains used in this study

Wild-type (NCIB361O)

eps mutant SSB488 (361O *epsA-O::tet*)

tasA mutant CA017 (361O *tasA::kan*)

sinReps double mutant (ZK4363)

Biofilm sample preparation

A 2 µl drop of bacterial cell suspension, grown as liquid culture overnight at 37 °C in Luria-Bertani (LB) medium, was spotted on solid MSgg medium agar (1.5%) plate [19], dried and kept at 30 °C or room temperature between 12 h – 10 days, as indicated in the text.

Spores sample preparation.

Wild-type *Bacillus subtilis* LB liquid culture, grown for 8 h at 37 °C, was spread (200 µl suspension) on solid LB agar (1.5%) plate and kept for 48 h at 37 °C.

TasA Purification and sample preparation.

TasA was purified as described previously [28,30]. Briefly, sinR eps double mutant *B.subtilis* cells (ZK4363) were grown in MSgg broth, at a 1:100 dilution from an LB overnight culture, under shaking conditions. After 16 h of growth at 37 °C the cells were pelleted (10000 g, 15 min, 4 °C), resuspended with saline extraction buffer and probe sonicated (1518 J, 5 s pulse and 2 s pulse off). Following an additional centrifugation step (10000 g, 15 min, 4 °C), the supernatant was then collected and filtered through a 0.45 µm polyethersulfone (PES) bottle-top filter. The filtered supernatant was collected after centrifugation (17000 g, 15 min, 4 °C), concentrated with Amicon centrifugal filter tubes and either

incubated in saline extraction buffer for 72 h at 4 °C (used to prepare 'TasA bundles') or passed through a HiLoad 26/60 Superdex S200 sizing column that was pre-equilibrated with a 50 mM NaCl, 5 mM HEPES solution at pH 8 (used to prepare 'TasA aggregates' and 'TasA fibrils'). Purified proteins were stored at −20 °C until use. The concentration of the protein was determined using a BCA protein assay (ThermoFisher Scientific, Waltham, MA, USA).

Polysaccharide purification

Polysaccharide was purified from WT Bacillus Subtilis pellicles, as previously described [12,32]. WT liquid culture was grown overnight in LB medium and transferred to SYN medium at a 1:100 dilution. Pellicles were collected after 24 h at 37 ˚C, transferred into fresh SYN medium and washed twice by centrifugation at 5000 rpm for 15 min at 25 ˚C. The pellet was collected probe sonicated (1518 J, 5 s pulse and 2 s pulse off) (Sonics, Vibra cell CV334) in fresh medium for 150 s. The supernatant was separated from the pellet after an additional sonication and centrifugation of 5000 rpm for 30 min at 25 ˚C. The EPS was precipitated by adding x3 ice-cold isopropanol (J.T. Baker) following an overnight at -20 ˚C. The supernatant was discarded and the precipitate was washed twice with ice-cold isopropanol and was kept at -20 ˚C for additional 2 h. The precipitant was collected, dissolved in 0.1 M MgCl2 (J.T. Baker) and extracted twice by phenol-chloroform (Fisher Chemical) on a separating funnel. The aqueous phase was collected, dialyzed for 48 h against DDW (with a Cellu Sep T3, 12000-14000 MWCO.) and lyophilized to dryness. For purification from DNA and proteins, EPS was dissolved in a 10 mM Tris buffer (VWR) containing 50 mM NaCl, 10 mM $MgCl_2$ pH 7.5 and incubated with DNase (Sigma-Aldrich) at 37 ˚C for 1 h. Proteinase K (Sigma-Aldrich) was then added and the solution was incubated at 40 ˚C for 1 h. The solution is dialyzed against DDW (with a Cellu Sep T3, 12000-14000 MWCO.) for 48 h and lyophilized to dryness.

TasA fibers preparation

TasA fibers were prepared as previously described [57], under the following conditions:

TasA bundles: Purified TasA was incubated in saline extraction buffer for 72 h at 4 °C. The solution was then dialyzed against TDW for three days, lyophilized and placed between two silicon nitride membrane or resuspended in a drop of water and mounted on a loop (Hampton Research).

TasA fibrils: Purified TasA was passed through a HiLoad 26/60 Superdex S200 sizing column that was pre-equilibrated with a 50 mM NaCl and 5 mM HEPES solution at pH 8. Sodium chloride stock solution (5M) was then added to the protein yielding the final concentration, 1.5 M NaCl and 130 µg/ml TasA. The solution was incubated for 72 h at 4 °C and dialyzed against TDW for three days, lyophilized and placed between two a silicon nitride membrane.

TasA aggregates: Purified TasA was passed through a HiLoad 26/60 Superdex S200 sizing column that was pre-equilibrated with a 50 mM NaCl and 5 mM HEPES solution at pH 8. The solution pH was then adjusted to 2.5 with formic acid, yielding TasA aggregates [56] and kept at room temperature for three days at 4 °C. The solution was exchanged by consecutive centrifugation (5000 rpm, 10 min) and supernatant replacement with TDW, three times every 24 h. The solution was then lyophilized and placed between two silicon nitride membranes or resuspended in a drop of water and mounted on a loop (Hampton Research).

Sample preparation for XRD measurements

Biofilm samples were mounted on aluminium frames overlaid with kapton films (13 µm thick from Goodfellow Cambridge limited or 25 µm thick from DuPont) or on a silicon nitride membrane (Silson Ltd., frame: 10.0 mm x 10.0 mm, 200 µm thick; membrane: 5.0 mm x 5.0 mm, 1000 nm thick). Hydrated biofilm measured at myspot was gently pulled off the agar plate, and sealed at the lab one hour prior to the measurement between two kapton films. During biofilm removal, only WT biofilms maintained their shape and humidity level. Fixed samples were prepared by overnight exposure to 15% formaldehyde vapour following mounting on kapton foil/Silicon nitride membrane.

Spore sample was scrapped from the plate and placed between Kapton sheets that were glued on an aluminium frame and sealed with a parafilm. Protein samples measured at ESRF were sandwiched between two 1000 nm thick silicon nitride membranes (see above).

SAXS/XRD and XRF mapping

Scanning XRD/XRF measurements of biofilms and proteins were performed at the mySpot beamline synchrotron BESSY II (Helmholtz Center, Berlin, Germany) and at the ID13 beamline Synchrotron ESRF (Grenoble, France).

At ID13 the X-ray beam (ESRF) was defined to 13.0 keV (0.954 Å) using Si(111) channel-cut monochromator and focused to 2.5 μm cross section. Scan steps varied between 2 μm or 5 μm. 2D patterns were acquired in transmission mode using a Dectris, EIGERr X 4M detector (pixel size 0.075x0.075 mm^2), by integrating for 2 s in an "on-the-fly" scanning mode. A Vortex EM, silicon drift detector with 50 mm^2 sensitive area, XRF detector was placed roughly 90°to the incoming X-ray beam to collect the emitted X-ray photons from the sample simultaneously. Acquisition time was set to 2 s/point.

At mySpot beamline the X-ray beam (Bessy II) was defined to 15.0 keV (0.827Å) using a B4C/Mo Multilayer monochromator and focused to (50x50) μm^2 using KB mirrors and 50 μm^2 pinhole. XRD data were obtained using a 2D Dectris Eiger 9 M detector ((2070 × 2167) $pixel^2$) in transmission geometry, and a single element Si(Li) XRF detector (RAYSPEC (SGX Sensortech) was placed perpendicular to the beam. Acquisition time was set to 60 s/point.

Sample to detector distance (around 300 mm) was calibrated using quartz powder in both setups. When present, internal kapton signal at q = 4 $nm^{-}1$ was used to further verify the calibration for each sample. Calibration of XRF detectors was performed using pyMCA (http://pymca.sourceforge.net/) using the argon emission and the main beam scattering energy. XRF intensities were corrected by the

theoretical absorption cross-section for each element, at 15 or 13 keV [46-49] taking into account (when relevant) the absorption of the XRF by the detector Beryllium window (8 µm thick).

SAXS/WAXS/XRF analysis.

Calibration, integration background removal, and peak-fitting of the 2D diffraction patterns were performed using the software DPDAK [65] or home-written routines based on pyFAI (https://pyfai.readthedocs.io/en/master/). The fitted parameters as well as the integrated XRF signal around specific emission lines, were exported and plotted in Origin 2020. For 1D presentation, the 1D patterns from specific regions of interest (ROI)s (X, Y, Z in Fig. 1E) were averaged and normalized by subtracting the minimum value and dividing by the maximum intensity.

The XRF maps were analysed using the software ImageJ [66]. Average atomic densities were extracted by analysing the calibrated grey-level histograms of relevant ROIs in the maps. The correction of the fluorescence intensity signal to relative atomic density was performed taking into account the absorption cross section at E=15 keV (Bessy II data), 13 keV (ESRF data) [46,47,49,67]. We note that absolute values cannot be quantitatively compared between beamline set ups and between sample as they depend amongst others on the incoming flux, the sample to detector distance and exact geometry, and the sample thickness.

Transmission Electron Microscopy of Biofilm colonies

Agar slabs (less than 0.5 mm^2) containing defined regions of the bacterial colonies were cut out and inverted on lecithin-coated 3-mm specimen carriers for high pressure freezing in a high-pressure freezing machine (Leica, ICE) with or without 10% polyvinylpyrrolidone as a filler (Δ*eps* biofilms and one of the WT samples were frozen without filler). Samples were transferred under liquid nitrogen into a freeze substitution unit (Leica, AFSII) with 0.1% osmium tetroxide in acetone for substitution medium. Samples were slowly warmed from -90 °C to 0 °C within 3 days.

The samples were washed with acetone for one hour and incubated with 0.5% uranyl acetate in acetone for 1 h still at 0 °C. Samples were washed 3x with acetone (moving from 0 °C to room temperature), before they were infiltrated with 25% and 50% epoxy resin (Roth, Germany) in acetone for 90 min. Samples were left in 75% epoxy resin overnight. Four changes of 100% epoxy resin followed over the period of 2 days before samples were flat-embedded between Teflon-coated microscope slides.

Infiltrated samples were polymerized at 60 °C for two days and defined regions mounted on resin stubs for cutting 70 nm–ultrathin cross-sections through the bacterial colonies, which were post-contrasted with 0.5 % uranyl acetate and 0.04% lead-citrate. Samples were investigated on a Morgagni transmission electron microscope (Thermofisher/FEI/Philips) at 80 kV and micrographs acquired with a Morada CCD camera (EmSis/Olympus) with ITEM software (EmSis/Olympus/Sys). Images were analysed using Fiji software [66]).

TEM images analysis according to cell type

Unbiased micrographs (image area (6 x 4.7) um with a 1.87 nm/px resolution) of the biofilm samples were acquired using the xy-coordinate display at the TEM, with a step size of 20 μm. Cells were marked and counted in these TEM images (N, total number of cells = 7159). Cell types were classified as normal cells, lysed cells, deformed cells, sporulating cells or spores as indicated in the text and in Fig. 4. The number of cells of each type was normalized by the number of images evaluated, which normalizes the total area that was probed. Normalizing by the area takes into account differences in cellular density and therefore we chose to normalize by area and not by total cell number.

Acknowledgments

Measurements were carried out at the mySpot beamline at the BESSY II electron storage ring operated by the Helmholtz-Zentrum Berlin für Materialien und Energie and at beamline ID13 at the European Synchrotron Radiation Facility. We thank the HBZ and the ESRF for provision of synchrotron radiation facilities and for financial support. We thank EM facility of MPI-CBG for support, use of equipment and reagents, Daniel Werner at the MPIKG for X-ray measurements. Jiliang Liu for ESRF ID13 beamline assistance at ESRF. Special thanks to Prof. Sigal Ben Yehuda for insightful discussions, Yosef Edery Aharony for his contribution with data sorting and image analysis and Daniel Rosenblatt for assistance with the image analysis. This work was funded by the Kaete Klausner scholarship.

References

1 Romeo, T. *Bacterial biofilms. Preface*. 1 edn, Vol. 322 (Springer-Verlag Berlin Heidelberg, 2008).

2 Costerton, J. W., Lewandowski, Z., Caldwell, D. E., Korber, D. R. & Lappin-Scott, H. M. MICROBIAL BIOFILMS. *Annual Review of Microbiology* **49**, 711-745, doi:10.1146/annurev.mi.49.100195.003431 (1995).

3 Branda, S. S., Vik, Å., Friedman, L. & Kolter, R. Biofilms: the matrix revisited. *Trends in microbiology* **13**, 20-26 (2005).

4 Flemming, H.-C. *et al.* Biofilms: an emergent form of bacterial life. *Nature Reviews Microbiology* **14**, 563-575, doi:10.1038/nrmicro.2016.94 (2016).

5 Boudarel, H., Mathias, J.-D., Blaysat, B. & Grédiac, M. Towards standardized mechanical characterization of microbial biofilms: analysis and critical review. *npj Biofilms and Microbiomes* **4**, 17, doi:10.1038/s41522-018-0062-5 (2018).

6 Wilking, J. N., Angelini, T. E., Seminara, A., Brenner, M. P. & Weitz, D. A. Biofilms as complex fluids. *MRS Bulletin* **36**, 385-391, doi:10.1557/mrs.2011.71 (2011).

7 Seminara, A. *et al.* Osmotic spreading of Bacillus subtilis biofilms driven by an extracellular matrix. *Proceedings of the National Academy of Sciences* **109**, 1116, doi:10.1073/pnas.1109261108 (2012).

8 Rubinstein, S. M. *et al.* Osmotic pressure can regulate matrix gene expression in Bacillus subtilis. *Mol Microbiol* **86**, 426-436, doi:10.1111/j.1365-2958.2012.08201.x (2012).

9 Ido, N. *et al.* Bacillus subtilis biofilms characterized as hydrogels. Insights on water uptake and water binding in biofilms. *Soft Matter* **16**, 6180-6190, doi:10.1039/D0SM00581A (2020).

10 Hobley, L. *et al.* BslA is a self-assembling bacterial hydrophobin that coats the Bacillus subtilis biofilm. *Proc Natl Acad Sci U S A* **110**, 13600-13605, doi:10.1073/pnas.1306390110 (2013).

11 Kobayashi, K. & Iwano, M. BslA(YuaB) forms a hydrophobic layer on the surface of Bacillus subtilis biofilms. *Mol Microbiol* **85**, 51-66, doi:10.1111/j.1365-2958.2012.08094.x (2012).

12 Azulay, D. N. *et al.* Biopolymers from a Bacterial Extracellular Matrix Affect the Morphology and Structure of Calcium Carbonate Crystals. *Crystal Growth & Design* **18**, 5582-5591, doi:10.1021/acs.cgd.8b00888 (2018).
13 Oppenheimer-Shaanan, Y. *et al.* Spatio-temporal assembly of functional mineral scaffolds within microbial biofilms. *npj Biofilms and Microbiomes* **2**, 15031, doi:10.1038/npjbiofilms.2015.31 (2016).
14 Nickel, J. C., Ruseska, I., Wright, J. B. & Costerton, J. W. Tobramycin resistance of Pseudomonas aeruginosa cells growing as a biofilm on urinary catheter material. *Antimicrob Agents Chemother* **27**, 619-624, doi:10.1128/aac.27.4.619 (1985).
15 McKenney, P. T., Driks, A. & Eichenberger, P. The Bacillus subtilis endospore: assembly and functions of the multilayered coat. *Nature Reviews Microbiology* **11**, 33-44, doi:10.1038/nrmicro2921 (2013).
16 Plomp, M., Carroll, A. M., Setlow, P. & Malkin, A. J. Architecture and Assembly of the Bacillus subtilis Spore Coat. *PLOS ONE* **9**, e108560, doi:10.1371/journal.pone.0108560 (2014).
17 Stöver, A. G. & Driks, A. Secretion, localization, and antibacterial activity of TasA, a Bacillus subtilis spore-associated protein. *Journal of bacteriology* **181**, 1664-1672 (1999).
18 Driks, A. Bacillus subtilis spore coat. *Microbiology and molecular biology reviews : MMBR* **63**, 1-20, doi:10.1128/MMBR.63.1.1-20.1999 (1999).
19 Branda, S. S., Gonzalez-Pastor, J. E., Ben-Yehuda, S., Losick, R. & Kolter, R. Fruiting body formation by Bacillus subtilis. *Proc Natl Acad Sci U S A* **98**, 11621-11626, doi:10.1073/pnas.191384198 (2001).
20 Vlamakis, H., Aguilar, C., Losick, R. & Kolter, R. Control of cell fate by the formation of an architecturally complex bacterial community. *Genes Dev* **22**, 945-953, doi:10.1101/gad.1645008 (2008).
21 O'Toole, G., Kaplan, H. B. & Kolter, R. Biofilm Formation as Microbial Development. *Annual Review of Microbiology* **54**, 49-79, doi:10.1146/annurev.micro.54.1.49 (2000).
22 Shapiro, J. A. THINKING ABOUT BACTERIAL POPULATIONS AS MULTICELLULAR ORGANISMS. *Annual Review of Microbiology* **52**, 81-104, doi:10.1146/annurev.micro.52.1.81 (1998).
23 Vlamakis, H., Chai, Y., Beauregard, P., Losick, R. & Kolter, R. Sticking together: building a biofilm the Bacillus subtilis way. *Nature Reviews Microbiology* **11**, 157-168, doi:10.1038/nrmicro2960 (2013).
24 Mukherjee, S. & Bassler, B. L. Bacterial quorum sensing in complex and dynamically changing environments. *Nat Rev Microbiol* **17**, 371-382, doi:10.1038/s41579-019-0186-5 (2019).
25 López, D., Vlamakis, H., Losick, R. & Kolter, R. Paracrine signaling in a bacterium. *Genes & development* **23**, 1631-1638, doi:10.1101/gad.1813709 (2009).
26 Bleich, R., Watrous, J. D., Dorrestein, P. C., Bowers, A. A. & Shank, E. A. Thiopeptide antibiotics stimulate biofilm formation in Bacillus subtilis. *Proc Natl Acad Sci U S A* **112**, 3086-3091, doi:10.1073/pnas.1414272112 (2015).
27 Drescher, K., Nadell, Carey D., Stone, Howard A., Wingreen, Ned S. & Bassler, Bonnie L. Solutions to the Public Goods Dilemma in Bacterial Biofilms. *Current Biology* **24**, 50-55, doi:10.1016/j.cub.2013.10.030 (2014).
28 Romero, D., Aguilar, C., Losick, R. & Kolter, R. Amyloid fibers provide structural integrity to Bacillus subtilis biofilms. *Proceedings of the National Academy of Sciences* **107**, 2230-2234 (2010).
29 Romero, D., Vlamakis, H., Losick, R. & Kolter, R. Functional Analysis of the Accessory Protein TapA in Bacillus subtilis Amyloid Fiber Assembly. *Journal of Bacteriology* **196**, 1505-1513, doi:10.1128/jb.01363-13 (2014).
30 Chai, L. *et al.* Isolation, characterization, and aggregation of a structured bacterial matrix precursor. *Journal of Biological Chemistry* **288**, 17559-17568 (2013).
31 El Mammeri, N. *et al.* Molecular architecture of bacterial amyloids in Bacillus biofilms. *FASEB J*, fj201900831R, doi:10.1096/fj.201900831R (2019).

32 Dogsa, I., Brloznik, M., Stopar, D. & Mandic-Mulec, I. Exopolymer diversity and the role of levan in Bacillus subtilis biofilms. *PLoS One* **8**, e62044, doi:10.1371/journal.pone.0062044 (2013).
33 Dragoš, A. *et al.* Division of Labor during Biofilm Matrix Production. *Current Biology* **28**, 1903-1913.e1905, doi:10.1016/j.cub.2018.04.046 (2018).
34 López, D., Vlamakis, H., Losick, R. & Kolter, R. Cannibalism enhances biofilm development in Bacillus subtilis. *Mol Microbiol* **74**, 609-618, doi:10.1111/j.1365-2958.2009.06882.x (2009).
35 Höfler, C. *et al.* Cannibalism stress response in Bacillus subtilis. *Microbiology (Reading, England)* **162**, 164-176, doi:10.1099/mic.0.000176 (2016).
36 Otto, S. B. *et al.* Privatization of Biofilm Matrix in Structurally Heterogeneous Biofilms. *mSystems* **5**, doi:10.1128/mSystems.00425-20 (2020).
37 Nadell, C. D., Drescher, K., Wingreen, N. S. & Bassler, B. L. Extracellular matrix structure governs invasion resistance in bacterial biofilms. *The ISME Journal* **9**, 1700-1709, doi:10.1038/ismej.2014.246 (2015).
38 Wilking, J. N. *et al.* Liquid transport facilitated by channels in Bacillus subtilis biofilms. *Proceedings of the National Academy of Sciences* **110**, 848, doi:10.1073/pnas.1216376110 (2013).
39 Qiu, X. & Setlow, P. Structural and Genetic Analysis of X-Ray Scattering by Spores of Bacillus subtilis. *Journal of Bacteriology* **191**, 7620-7622, doi:10.1128/JB.01200-09 (2009).
40 Jakubovics, N. S., Shields, R. C., Rajarajan, N. & Burgess, J. G. Life after death: the critical role of extracellular DNA in microbial biofilms. *Letters in applied microbiology* **57**, 467-475, doi:10.1111/lam.12134 (2013).
41 Zuo, X. *et al.* X-ray diffraction “fingerprinting” of DNA structure in solution for quantitative evaluation of molecular dynamics simulation. *Proceedings of the National Academy of Sciences of the United States of America* **103**, 3534, doi:10.1073/pnas.0600022103 (2006).
42 Phan-Xuan, T. *et al.* Hydration-Induced Structural Changes in the Solid State of Protein: A SAXS/WAXS Study on Lysozyme. *Molecular Pharmaceutics* **17**, 3246-3258, doi:10.1021/acs.molpharmaceut.0c00351 (2020).
43 Skinner, L. B. *et al.* Benchmark oxygen-oxygen pair-distribution function of ambient water from x-ray diffraction measurements with a wide Q-range. *The Journal of Chemical Physics* **138**, 074506, doi:10.1063/1.4790861 (2013).
44 Bodík, M. *et al.* Diffraction pattern of Bacillus subtilis CotY spore coat protein 2D crystals. *Colloids and surfaces. B, Biointerfaces* **197**, 111425, doi:10.1016/j.colsurfb.2020.111425 (2021).
45 Kadota, H. & Iijima, K. The X-ray Diffraction Pattern of Spores of Bacillus subtilis. *Agricultural and Biological Chemistry* **29**, 80-81, doi:10.1080/00021369.1965.10858352 (1965).
46 Scofield, J. H. Relativistic hartree-slater values for K and L X-ray emission rates. *Atomic Data and Nuclear Data Tables* **14**, 121-137, doi:https://doi.org/10.1016/S0092-640X(74)80019-7 (1974).
47 Scofield, J. H. Theoretical photoionization cross sections from 1 to 1500 keV. 376 (United States, 1973).
48 Onder, P., Tursucu, A. & Demir, D. K Shell X-Ray Fluorescence Parameters of Some Elements in the Atomic Range. *Science and Technology of Nuclear Installations* **2013**, 285190, doi:10.1155/2013/285190 (2013).
49 Krause, M. O. Atomic radiative and radiationless yields for K and L shells. *Journal of Physical and Chemical Reference Data* **8**, 307-327, doi:10.1063/1.555594 (1979).
50 Nishikawa, M., Kobayashi, K. & Henkin Tina, M. Calcium Prevents Biofilm Dispersion in Bacillus subtilis. *Journal of Bacteriology* **203**, e00114-00121, doi:10.1128/JB.00114-21.
51 Kwak, M.-K., Ryu, H.-B., Song, S.-H., Lee, J.-W. & Kang, S.-O. Anti-σ factor YlaD regulates transcriptional activity of σ factor YlaC and sporulation via manganese-dependent redox-

sensing molecular switch in Bacillus subtilis. *Biochemical Journal* **475**, 2127-2151, doi:10.1042/bcj20170911 (2018).

52 Chung, P. Y. & Khanum, R. Antimicrobial peptides as potential anti-biofilm agents against multidrug-resistant bacteria. *Journal of Microbiology, Immunology and Infection* **50**, 405-410, doi:https://doi.org/10.1016/j.jmii.2016.12.005 (2017).

53 Eisenberg, D. S. & Sawaya, M. R. Structural Studies of Amyloid Proteins at the Molecular Level. *Annual Review of Biochemistry* **86**, 69-95, doi:10.1146/annurev-biochem-061516-045104 (2017).

54 Diehl, A. *et al.* Structural changes of TasA in biofilm formation of Bacillus subtilis. *Proc Natl Acad Sci U S A* **115**, 3237-3242, doi:10.1073/pnas.1718102115 (2018).

55 Erskine, E. *et al.* Formation of functional, non-amyloidogenic fibres by recombinant Bacillus subtilis TasA. *Mol Microbiol* **110**, 897-913, doi:10.1111/mmi.13985 (2018).

56 Azulay, D. N. *et al.* Colloidal-like aggregation of a functional amyloid protein. *Physical Chemistry Chemical Physics* **22**, 23286-23294, doi:10.1039/D0CP03265D (2020).

57 Ghrayeb, M., Hayet, S., Lester-Zer, N., Levi-Kalisman, Y. & Chai, L. Fibrilar Polymorphism of the Bacterial Extracellular Matrix Protein TasA. *Microorganisms* **9**, 529 (2021).

58 Sawaya, M. R. *et al.* Atomic structures of amyloid cross-[bgr] spines reveal varied steric zippers. *Nature* **447**, 453-457, doi:http://www.nature.com/nature/journal/v447/n7143/suppinfo/nature05695_S1.html (2007).

59 Li, B. *et al.* Cryo-EM of full-length α-synuclein reveals fibril polymorphs with a common structural kernel. *Nature Communications* **9**, 3609, doi:10.1038/s41467-018-05971-2 (2018).

60 Nelson, R. *et al.* Structure of the cross-[beta] spine of amyloid-like fibrils. *Nature* **435**, 773-778, doi:http://www.nature.com/nature/journal/v435/n7043/suppinfo/nature03680_S1.html (2005).

61 Chandrangsu, P., Rensing, C. & Helmann, J. D. Metal homeostasis and resistance in bacteria. *Nature Reviews Microbiology* **15**, 338-350, doi:10.1038/nrmicro.2017.15 (2017).

62 van Hullebusch, E. D., Zandvoort, M. H. & Lens, P. N. L. Metal immobilisation by biofilms: Mechanisms and analytical tools. *Reviews in Environmental Science and Biotechnology* **2**, 9-33, doi:10.1023/B:RESB.0000022995.48330.55 (2003).

63 Chung, L., Rajan, K. S., Merdinger, E. & Grecz, N. Coordinative Binding of Divalent Cations with Ligands Related to Bacterial Spores: Equilibrium Studies. *Biophysical Journal* **11**, 469-482, doi:https://doi.org/10.1016/S0006-3495(71)86229-X (1971).

64 Granger, A. C., Gaidamakova, E. K., Matrosova, V. Y., Daly, M. J. & Setlow, P. Effects of Mn and Fe levels on Bacillus subtilis spore resistance and effects of Mn2+, other divalent cations, orthophosphate, and dipicolinic acid on protein resistance to ionizing radiation. *Appl Environ Microbiol* **77**, 32-40, doi:10.1128/AEM.01965-10 (2011).

65 Benecke, G. *et al.* A customizable software for fast reduction and analysis of large X-ray scattering data sets: applications of the new DPDAK package to small-angle X-ray scattering and grazing-incidence small-angle X-ray scattering. *Journal of applied crystallography* **47**, 1797-1803, doi:10.1107/s1600576714019773 (2014).

66 Schindelin, J. *et al.* Fiji: an open-source platform for biological-image analysis. *Nature Methods* **9**, 676-682, doi:10.1038/nmeth.2019 (2012).

67 Onder, P., Tursucu, A. & Demir, D. K Shell X-Ray Fluorescence Parameters of Some Elements in the Atomic Range. *Science and Technology of Nuclear Installations* **2013**, 1-6, doi:10.1155/2013/285190 (2013).